Broadband operation of rolled-up hyperlenses

Stephan Schwaiger, Andreas Rottler, Markus Bröll, Jens Ehlermann, Andrea Stemmann, Daniel Stickler, Christian Heyn, Detlef Heitmann, and Stefan Mendach*

Institut für Angewandte Physik und Mikrostrukturforschungszentrum, Universität Hamburg, Jungiusstrasse 11, D-20355 Hamburg, Germany

(Received 19 December 2011; revised manuscript received 29 February 2012; published 13 June 2012)

This work is related to an earlier publication [Schwaiger *et al.*, Phys. Rev. Lett. **102**, 163903 (2009)], where we demonstrated by means of fiber-based transmission measurements that rolled-up Ag-(In)GaAs multilayers represent three-dimensional metamaterials with a plasma edge which is tunable over the visible and near-infrared regime by changing the thickness ratio of Ag and (In)GaAs, and predicted by means of finite-difference time-domain simulations that hyperlensing occurs at this frequency-tunable plasma edge. In the present work we develop a method to measure reflection curves on these structures and find that they correspond to the same tunable plasma edge. We find that retrieving the effective parameters from transmission and reflection data fails, because our realized metamaterials exceed the single-layer thicknesses of 5 nm, which we analyze to be the layer thickness limit for the applicability of effective parameter retrieval. We show that our realized structures nevertheless have the functionality of an effective metamaterial by supplying a detailed finite-difference time-domain study which compares light propagation through our realized structure (17-nm-thick Ag layers and 34-nm-thick GaAs layers) and light propagation through an idealized structure of the same total thickness but with very thin layers [2-nm-thick Ag layers and 4-nm-thick (In)GaAs layers]. In particular, our simulations predict broadband hyperlensing covering a large part of the visible spectrum for both the idealized and our realized structures.

DOI: 10.1103/PhysRevB.85.235309 PACS number(s): 81.05.Xj, 78.67.Pt

I. INTRODUCTION

Optical cloaking,[1–5] subwavelength imaging,[6–12] or a negative index of refraction[13–18] can be realized using metamaterials. These artificially designed materials are constructed from subwavelength unit cells usually consisting of metal and dielectric. Their effective optical properties can be tailored in a wide range not accessible by natural materials. Subwavelength imaging using metamaterials was proposed a decade ago[19] and realized using a thin slab of metal[9,20] or metal/dielectric multilayers.[8,21,22] In order to examine subwavelength objects with conventional optics it was proposed that curved multilayers of metal and dielectric exhibit an anisotropic permittivity and can be used to project the subwavelength details of objects to the far field.[23] These hyperlenses were realized using curved layers of Ag and oxides with an operation frequency in the ultraviolet and violet regime.[11,12] By use of rolled-up metal/semiconductor superlattices the operation frequency could be pushed to the visible and near-infrared regime.[24–26]

In Ref. 24 we demonstrated the principle of operation and the functionality of a rolled-up metal-semiconductor hyperlens (RHL) by means of transmission measurements and finite-difference time-domain simulations. In this article we extend the study. We develop a method to obtain reflection data and present detailed reflection and transmission measurements. We observe metallic reflection at low photon energies and dielectric transmission at high photon energies. The transition between these two regimes, the plasma edge, is characterized by the effective plasma frequency of the RHL. Furthermore, we apply a parameter retrieval method to obtain the effective permittivity of the investigated structures from the reflection and transmission measurements. Comparing the retrieved data with an effective-medium model for metal/semiconductor superlattices,[21] we find strong deviations. Theoretical investigations show that the effective parameter retrieval method is not applicable if the individual layer thicknesses exceed 5–10 nm, which is the case for our realized structures. However, finite-difference time-domain simulations reveal that subwavelength imaging occurs not only for idealized structures with very thin layers, but also for layer thicknesses of $d_{\mathrm{Ag}} = 17\,\mathrm{nm}$ and $d_{(\mathrm{In})\mathrm{GaAs}} = 34\,\mathrm{nm}$, which have been used in the experiments. In addition, for the realized and experimentally investigated structures as well as on optimized structures, the simulations show that efficient subwavelength imaging occurs for frequencies not only at the effective plasma frequency, but also at higher frequencies. Our findings show that the functionality of a metamaterial might still be obtained when the effective parameter retrieval does not work for that material.

II. MODELS

In this section we give an overview of the analytical models which are used in this paper to theoretically describe the RHL. These models are (a) the transfer-matrix ansatz and (b) the effective-medium model.

(a) Since the RHL represents a superlattice consisting of alternating layers of metal (Ag) and semiconductor ((In)GaAs), one can use a transfer-matrix ansatz to calculate the reflection R and transmission T through the structure.[27] For these calculations, the layers have been assumed to be planar [see Fig. 1(a)]. The Ag has an individual layer thickness of d_{Ag} and the (In)GaAs bilayer exhibits a thickness of $d_{(\mathrm{In})\mathrm{GaAs}}$. The permittivity of (In)GaAs is approximated with the permittivity of GaAs, ϵ_{GaAs}. Both permittivities ϵ_{Ag} and ϵ_{GaAs} are linear interpolations of experimental data presented by Palik.[28]

(b) A structure consisting of alternating layers of Ag and (In)GaAs with individual layer thicknesses d_{Ag} and $d_{(\mathrm{In})\mathrm{GaAs}}$ that are much smaller than the wavelength of the

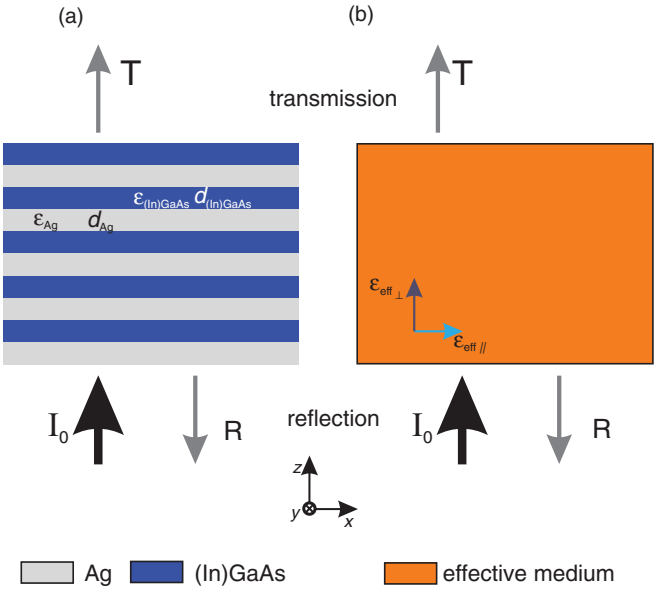

FIG. 1. (Color online) (a) Planar superlattice of Ag and GaAs layers with permittivities ϵ_{Ag} and $\epsilon_{(In)GaAs}$, and individual layer thicknesses d_{Ag} and $d_{(In)GaAs}$. The transmission and reflection through such a structure can be calculated with a transfer-matrix ansatz. I_0 marks the incident radiation and R and T denote the reflected and transmitted fields, respectively. (b) If d_{Ag} and $d_{(In)GaAs}$ are much smaller than the wavelength of the incident radiation, the structure can be modeled as an effective medium with parallel ($\epsilon_{eff||}$) and perpendicular ($\epsilon_{eff\perp}$) permittivity components.

incident radiation can be modeled as a homogeneous medium [Fig. 1(b)]. The effective permittivity of the structure is described by an anisotropic tensor with components $\epsilon_{eff||}$ and $\epsilon_{eff\perp}$, denoting the permittivity parallel and perpendicular to the layers. These permittivities read as

$$\epsilon_{eff||} = \frac{\epsilon_{GaAs} + \eta\epsilon_{Ag}}{1+\eta}, \tag{1}$$

$$\frac{1}{\epsilon_{eff\perp}} = \frac{1}{1+\eta}\left(\frac{1}{\epsilon_{GaAs}} + \frac{\eta}{\epsilon_{Ag}}\right), \tag{2}$$

where $\eta = \frac{d_{Ag}}{d_{(In)GaAs}}$ is the layer thickness ratio between the Ag layer and the GaAs layer.[21,29,30] The total structure thickness d_{tot} of the effective medium is assumed to be the sum of the thicknesses of all individual layers, i.e., $d_{tot} = \sum_i d_i$.

Within the framework of the effective-medium model an effective plasma frequency $\omega_{p\,eff}$ can be applied to the multilayered structure by the following equation:

$$\epsilon_{eff||}(\omega_{p\,eff}) = 0. \tag{3}$$

At the plasma frequency $\omega_{p\,eff}$ the multilayered structure exhibits a flat isofrequency surface, allowing the structure to be utilized as a subwavelength imaging device; see, e.g., Ref. 8. We derive the effective plasma frequency $\omega_{p\,eff}$ of our RHLs from transmission and reflection measurements presented in Sec. V. We furthermore apply the effective parameter retrieval to reflection and transmission data of the RHL to discuss the deviations for the effective-medium model in Sec. VI.

III. INVESTIGATED SAMPLES

The samples investigated experimentally are fabricated using the self-rolling principle of strained layers.[31,32] Using molecular-beam epitaxy the following layers are grown onto a GaAs substrate: a GaAs buffer layer (100 nm), an AlAs sacrificial layer (40 nm), a strained $In_{20}Ga_{80}As$ layer (17 nm), and an unstrained GaAs layer (17 nm). Subsequently a Ag layer, which is varied in different samples between $d_{Ag} = 17$ nm and $d_{Ag} = 25$ nm, is deposited using thermal evaporation. When the sacrificial layer is removed with a selective etchand (HF acid) the system minimizes its strain energy, causing the layers to roll up into a microtube with radii which are tailored in our experiments between $r = 1.5\,\mu$m and $r = 4\,\mu$m. The number of layers can be adjusted by the time the sample is exposed to the selective etchand. In one fabrication sequence we produce about 100 microtubes. The yield of compactly rolled microtubes on one sample decreases with the included number of rotations. Compactly rolled-up microtubes with up to seven rotations have been obtained.

Figure 2(a) shows a scanning electron micrographic (SEM) image of a rolled-up microtube. The microtube exhibits a radius of $r = 4\,\mu$m and consists of four alternating layers of Ag ($d_{Ag} = 17$ nm) and (In)GaAs ($d_{(In)GaAs} = 34$ nm). The length of the microtube is $l = 75\,\mu$m. This microtube is named $RHL_{0.5}$ and investigated using transmission and reflection measurements in Sec. V. To demonstrate the quality of our RHLs we examine several RHLs using SEM imaging. One RHL chosen as an example is presented in Fig. 2(b). The RHL exhibits seven alternating layers of Ag and (In)GaAs and an inner radius of $r_{inner} = 1.5\,\mu$m. We prepared two cross sections into the outer perimeter of the RHL using focused ion beams, one complete cut through the structure in the vicinity of one end of the RHL (cross section 1) and one rectangular hole in the upper perimeter of the RHL (cross section 2). Cross section 1 indicates that no gaps between the single layers occur at the upper perimeter while at the sidewalls gaps are visible. This

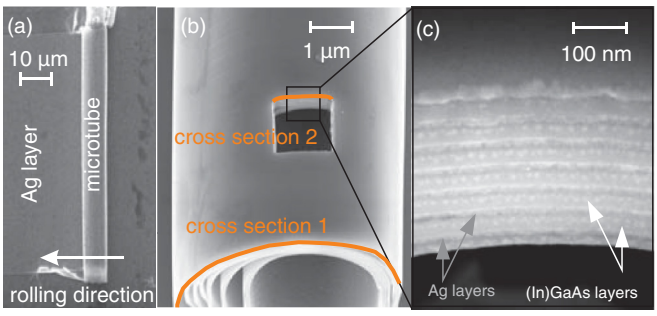

FIG. 2. (Color online) Scanning electron micrograph of rolled-up hyperlenses (RHLs). (a) A Ag layer is deposited onto a strained semiconductor system. By rolling up the planar layers we achieve a microtube with multiple rotations which represents a RHL. (b) To examine the quality of a RHL we cut two cross sections (cross sections 1 and 2) into the RHL using focused ion beams. The position of the cross section 2 corresponds to a position at which optical experiments are performed. (c) A side view of the cross section 2 far enough away from the edge of the microtube shows that the RHL exhibits a well-defined radial superlattice of metal and semiconductor at its upper perimeter.

observation is confirmed to be representative by investigations on several RHLs. Cross section 2 is located at a position at which optical transmission and reflection measurement are usually carried out. In the magnification of cross section 2 [Fig. 2(c)] it is clearly visible that no gaps between the single layers occur. The upper perimeter of the RHL represents a high-quality compact superlattice of Ag and (In)GaAs.

We investigate the transmission through and the reflection on four different RHLs with the same semiconductor thickness $d_{(\mathrm{In})\mathrm{GaAs}} = 34$ nm and different Ag thicknesses. The Ag thickness is $d_{\mathrm{Ag}} = 17$ nm ($d_{\mathrm{Ag}} = 19$ nm, $d_{\mathrm{Ag}} = 22$ nm, $d_{\mathrm{Ag}} = 25$ nm) and the number of rotations is 4 (4, 6, 5). We name the rolled-up hyperlenses RHL_{η}, according to their layer thickness ratio between the Ag layer and the GaAs layer, $\eta = \frac{d_{\mathrm{Ag}}}{d_{(\mathrm{In})\mathrm{GaAs}}}$: $\mathrm{RHL}_{0.5}$, $\mathrm{RHL}_{0.56}$, $\mathrm{RHL}_{0.65}$, and $\mathrm{RHL}_{0.74}$. Consequently the total thickness of $\mathrm{RHL}_{0.5}$ ($\mathrm{RHL}_{0.56}$, $\mathrm{RHL}_{0.65}$, $\mathrm{RHL}_{0.74}$) is $d_{\mathrm{total}} = 204$ nm ($d_{\mathrm{total}} = 212$ nm, $d_{\mathrm{total}} = 336$ nm, $d_{\mathrm{total}} = 295$ nm).

IV. MEASUREMENT SETUPS

The optical properties of the RHLs are investigated using a reflection measurement setup as well as a transmission measurement setup. The reflection measurement setup is sketched in Fig. 3(a). We measure the reflection on the upper perimeter of a RHL. In detail, white light ($E_{\mathrm{ph}} < 1$ eV to $E_{\mathrm{ph}} = 2.6$ eV) from a supercontinuum white-light source is focused to the back focal plane of a 50× objective. Consequently the sample placed in the focus of the objective is illuminated homogeneously with white light. The reflected

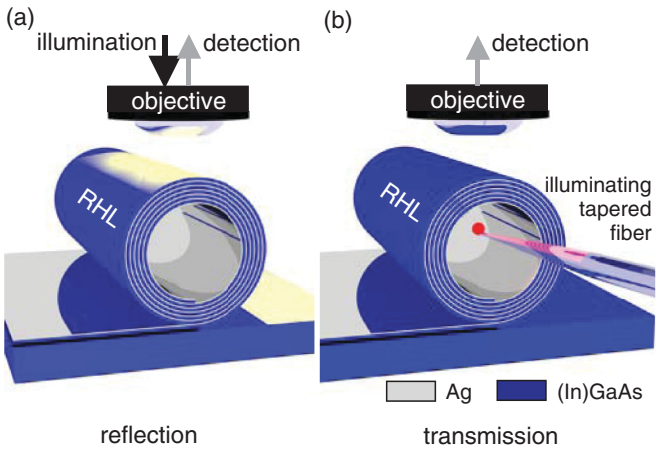

FIG. 3. (Color online) Sketch of the measurement techniques used to investigate the optical properties of a RHL consisting of alternating layers of Ag and (In)GaAs. (a) For performing reflection measurements the RHL is illuminated homogeneously with white light using a microscope setup. The reflected light is collected with a microscope objective and analyzed using a spectrometer in combination with a charge coupled device (CCD) camera. (b) The transmission through a RHL is measured using a fiber-based transmission measurement setup. A tapered optical fiber emits light perpendicular to its orientation through a hole in the sidewall. It can be manipulated inside a RHL to illuminate it from the inside. Subsequently the transmitted light is detected with a microscope setup and a CCD camera.

light is collected with the same objective and divided into two beams using a beam splitter. Subsequently the two beams are focused to create two image planes of the sample. In one image plane we position a camera which allows the sample to be viewed. In the other image plane we position a movable optical multimode fiber with a core diameter of 100 μm. The other end of the fiber is placed into the entrance of a spectrometer, which disperses the collected light and focuses it onto a nitrogen-cooled charge-coupled device (CCD) camera. Using this setup we are able to collect the light, depending on its photon energy E, reflected from a well-defined and selectable area with a diameter of 2 μm on the sample. To achieve a reflection spectrum of a RHL microtube we measure the intensity of the light reflected from the microtube's outer surface. Subsequently we normalize the intensity by placing a Ag mirror in the position of the RHL and measuring the intensity reflected from the Ag mirror. In the normalization the reflectivity of the Ag mirror is taken into account. It is worth mentioning that in the first experiments we focused the white light directly onto a spot on the RHL. It turned out that the shape of this spot varied with the energy of the light, and a reliable reflection measurement was possible only when the sample was illuminated homogeneously.

The transmission measurements are carried out using a fiber-based transmission measurement setup as sketched in Fig. 3(b). As a light source we utilize a tapered optical fiber with a tip diameter of $d_{\mathrm{tip}} \approx 1$ μm. The tapered fiber tip was metallized homogeneously with AuPd. Subsequently we drill a hole into the metallization of the tip using focused ion beams. Monochromatic light provided by a supercontinuum white-light source in combination with a monochromator is coupled into the untapered end of the tapered fiber, guided to its tip, and emitted from the hole in the sidewall at the tip. The emitted light is then transmitted through the RHL and collected using a microscope objective. The collected light is focused onto the sensitive area of a CCD camera. We achieve a spectrum of the light transmitted through the RHL by scanning the energy of the light. In the next step we normalize the spectrum by removing the light-emitting fiber tip from the RHL and acquiring a spectrum of the light emitted from the fiber tip without being transmitted through the RHL.

V. MEASUREMENTS

In Fig. 4(a) we present reflection and transmission measurements on $\mathrm{RHL}_{0.5}$, consisting of four double layers of Ag ($d_{\mathrm{Ag}} = 17$ nm) and (In)GaAs ($d_{(\mathrm{In})\mathrm{GaAs}} = 34$ nm). At a photon energy of $E_{\mathrm{ph}} = 1.4$ eV the reflection is $R \approx 1$. Towards higher photon energy the reflection R decreases while the transmission T increases. Both reflection R and transmission T start to oscillate at photon energies above $E \approx 1.8$ eV. The two maxima in transmission T_{max} at photon energies of $E = 1.76$ eV and $E = 2.13$ eV correspond to two minima in the reflection R_{min} at $E = 1.76$ eV and $E = 2.1$ eV, respectively. At photon energies above $E \approx 2.2$ eV the transmission T decreases again while the reflection is $R \approx 60\%$.

The decrease of transmission T towards high photon energies can be explained by an increase of absorption in the (In)GaAs compound of the RHL. The decrease of transmission T and the corresponding increase of reflection R towards

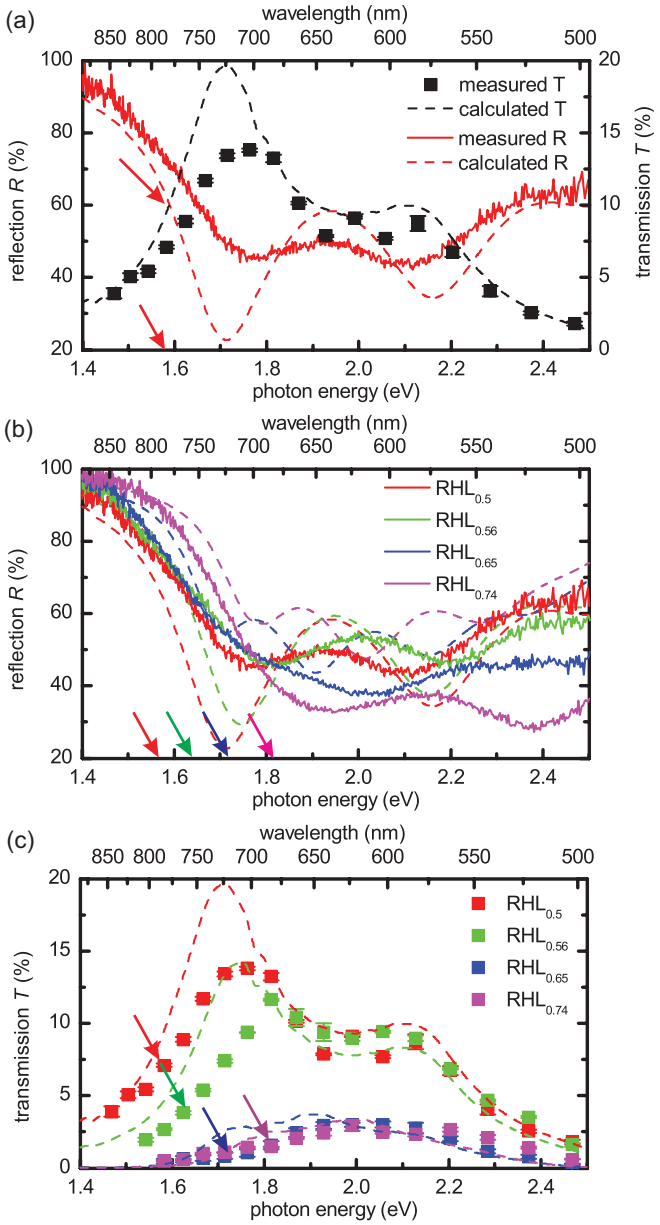

FIG. 4. (Color online) (a) Measured reflection (solid line) and transmission (squares) of $RHL_{0.5}$ and the corresponding transfer-matrix calculation of the multilayer system (dashed lines) plotted against the photon energy E. At low photon energies $RHL_{0.5}$ exhibits metallic reflection. With increasing photon energy $RHL_{0.5}$ shows dielectric transmission. The transition between the these two regimes is characterized by the plasma frequency $\omega_{\mathrm{p\,eff}}$ (red arrow). (b) Measured reflection (solid lines) of four RHLs with different layer thickness ratios and the corresponding transfer-matrix calculations (dashed lines). The arrows point to the plasma frequency $\omega_{\mathrm{p\,eff}}$ of the corresponding RHL. (c) Measured transmission (symbols) of the same RHLs and the corresponding transfer matrix calculations (dashed lines). The transition from metallic reflection to dielectric transmission characterized by the plasma frequency $\omega_{\mathrm{p\,eff}}$ can be tuned by varying the layer thickness ratio η of the RHLs.

low photon energies represent a transition of the RHL from dielectric transmission to metallic reflection. This transition can be characterized by the energy $E_{R/2}$, the energy where the reflection has decreased to a value exactly between the value of the minimum R_{min} and $R = 1$, or the energy $E_{T/2}$ where the transmission has increased to half the value of the maximum, $\frac{T_{\mathrm{max}}}{2}$. For $RHL_{0.5}$ these values are $E_{R/2} = 1.58$ eV and $E_{T/2} = 1.58$ eV. By comparing these values with the energy of the plasma frequency of the effective medium, $\hbar\omega_{\mathrm{p\,eff}} = 1.57$ eV [marked with a red arrow in Fig. 4(a)] we find a good agreement, showing that the effective plasma frequency $\omega_{\mathrm{p\,eff}}$ is an appropriate quantity to understand the transition between the regime of dielectric transmission and the regime of metallic reflection of a RHL.

In the next step we model our data with transfer-matrix calculations as introduced in Sec. II. We consider a realistic multilayer structure with the individual layer thicknesses d_{Ag} and $d_{\mathrm{(In)GaAs}}$. The calculations, shown in Fig. 4(a) (dashed lines), confirm the general behavior of the experimental results. The decrease of transmission and the corresponding increase of reflection towards low energies are clearly visible. However, the oscillation of transmission and reflection in the energy range from $E \approx 1.6$ eV to $E \approx 2.2$ eV are more pronounced in the calculations than in the experiment. These oscillations can be attributed to Fabry-Pérot resonances in the total thickness of the RHL and were studied in detail in Ref. 33. It was shown that by varying the number of rotations of the RHL, Fabry-Pérot resonances can be used to optimize the transmission of a RHL at a desired frequency.

In order to investigate whether the deviation between the calculations and the experiment can be attributed to varying angles of incidences when light is transmitted through the RHL, we performed the following experiments. We replaced the 50× objective in the transmission measurement setup with a 10× objective. Due to the different numerical aperture of the 10× objective, we collect light from a smaller range of angles as compared to the 50× objective. In performing transmission measurements through the RHL using the 50× objective and the 10× objective, we did not find significant differences. We furthermore can exclude an underestimation of the absorption in the semiconductor layers as the reason for the deviation between experiments and calculations, because the measured decrease of transmission towards high photon energies, which is mainly caused by the absoption in the semiconductor, is well confirmed by the calculations. We attribute the deviations between calculations and experimental data to surface roughnesses of the thin Ag layers which cause the Fabry-Pérot resonances that occur to be less pronounced in the experiment.

In Fig. 4(b) we present reflection measurements on the four RHLs introduced in Sec. III with different layer thickness ratios η and the corresponding theory using transfer-matrix calculations. At a photon energy of $E_{\mathrm{ph}} = 1.4$ eV the reflection of all four samples exhibits $R \approx 1$. Towards higher photon energy the reflection decreases and starts oscillating at photon energies of $E_{\mathrm{ph}} \approx 1.8$ eV. We now focus on the energy $E_{R/2}$ which characterizes the plasma frequency of the RHL. For $RHL_{0.5}$ ($RHL_{0.56}$, $RHL_{0.65}$, $RHL_{0.74}$) this energy is $E_{R/2} = 1.58$ eV ($E_{R/2} = 1.59$ eV, $E_{R/2} = 1.62$ eV, $E_{R/2} = 1.69$ eV). $E_{R/2}$ and with it the plasma frequency of the effective material $\omega_{\mathrm{p\,eff}}$ [marked with colored arrows in Fig. 4(a)] increases with increasing layer thickness ratio and percentage of Ag in the RHL.

In Fig. 4(c) we present transmission measurements on the same RHL on which we performed the reflection

measurements and the corresponding transfer-matrix calculations. Now we focus on the energy $E_{T/2}$. For $RHL_{0.5}$ ($RHL_{0.56}$, $RHL_{0.65}$, $RHL_{0.74}$) this energy is $E_{T/2} = 1.58$ eV ($E_{T/2} = 1.68$ eV, $E_{T/2} = 1.81$ eV, $E_{T/2} = 1.81$ eV). The trend that the energy $E_{T/2}$ and with it the plasma frequency of the effective material $\omega_{\mathrm{p\,eff}}$ increases with increasing layer thickness ratio η is confirmed.

In conclusion the effective plasma frequency $\omega_{\mathrm{p\,eff}}$ characterized by the value $E_{R/2}$ or $E_{T/2}$ can be tuned with increasing layer thickness ratio η to higher photon energies E. In accordance with the conclusions drawn in Ref. 24, the RHL is an effective material with a plasma frequency $\omega_{\mathrm{p\,eff}}$ in the visible and near-infrared regime which divides the frequency regimes of high reflectance and of dielectric transmission.

VI. RETRIEVAL OF THE PARAMETERS FOR THE EFFECTIVE-MEDIUM MODEL

In this section we will focus on the retrieval of the effective optical parameters of the RHL. We therefore assume the RHL to be a planar effective medium with thickness d_{tot} and effective permittivity components $\epsilon_{\mathrm{eff}||}$ and $\epsilon_{\mathrm{eff}\perp}$, as outlined in Sec. II. On both ends the effective medium is supposed to be surrounded by air with a permittivity $\epsilon_{\mathrm{out}} = 1$. Since the multilayers are supposed to be infinite in two dimensions, the inductivity should be zero, preventing the magnetic field from coupling to the structure. Therefore we have to set $\mu = 1$. We assume perpendicular incidence of the light in the experiment, i.e., $\vec{k} = (0,0,k_z)$. Consequently, only the permittivity component parallel to the surface ($\epsilon_{\mathrm{eff}||}$) influences the transmission and reflection spectra. Regarding the dispersion relation $\vec{k}^2 = \epsilon_0\mu_0\epsilon\mu\omega^2$, we can write k_z outside the structure as $k_{z,\mathrm{out}} = \omega/c_0$, where $c_0 = 1/\sqrt{\epsilon_0\mu_0}$ is the vacuum light velocity, ω is the angular frequency, and $\epsilon = \epsilon_{\mathrm{out}} = 1$. The effective permittivity inside the structure can be written as $\epsilon = \epsilon_{\mathrm{eff}||} = \epsilon'_{\mathrm{eff}||} + i\epsilon''_{\mathrm{eff}||}$, where $\epsilon'_{\mathrm{eff}||}$ and $\epsilon''_{\mathrm{eff}||}$ denote the real and imaginary part, respectively. Hence k_z inside the effective medium reads

$$k_z = k_z(\omega,\epsilon'_{\mathrm{eff}||},\epsilon''_{\mathrm{eff}||}) = \frac{\omega}{c_0}\sqrt{\epsilon'_{\mathrm{eff}||} + i\epsilon''_{\mathrm{eff}||}}. \tag{4}$$

Calculating analytically the reflection and transmission coefficients through the structure, as in a Fabry-Pérot interferometer, one can derive formulas that connect the real and imaginary parts of $\epsilon_{\mathrm{eff}||}$ to the measured reflection and transmission. These formulas read as

$$R = |r_{012}(\omega,\epsilon'_{\mathrm{eff}||},\epsilon''_{\mathrm{eff}||})|^2, \tag{5}$$

$$T = |t_{012}(\omega,\epsilon'_{\mathrm{eff}||},\epsilon''_{\mathrm{eff}||})|^2, \tag{6}$$

where r_{012} and t_{012} are the reflection and transmission coefficients through the entire slab, respectively. We remark that for a given layer thickness d_{tot} the coefficients r_{012} and t_{012} depend only on the variables ω, $\epsilon'_{\mathrm{eff}||}$, and $\epsilon''_{\mathrm{eff}||}$, i.e., $r_{012}(\omega,\epsilon'_{\mathrm{eff}||},\epsilon''_{\mathrm{eff}||})$, $t_{012}(\omega,\epsilon'_{\mathrm{eff}||},\epsilon''_{\mathrm{eff}||})$. Equations (5) and (6) therefore form a system of equations with variables $\epsilon'_{\mathrm{eff}||}$ and $\epsilon''_{\mathrm{eff}||}$ that can be solved for given frequencies ω. For the solution process we use a root-finding algorithm of the commercial software MATHEMATICA.[34]

Figure 5(a) shows the retrieved real (upper graph) and imaginary (lower graph) parts of $\epsilon_{\mathrm{eff}||}$ for the structure with a layer thickness ratio $\eta = 0.5$ ($RHL_{0.5}$). The solid black lines show $\epsilon'_{\mathrm{eff}||}$ and $\epsilon''_{\mathrm{eff}||}$ calculated from the effective-medium model. It can be seen that the structure has the plasma frequency $\omega_{\mathrm{p\,eff}}$ at an energy $\hbar\omega_{\mathrm{p\,eff}} = 1.57$ eV. The red dots depict the retrieved $\epsilon'_{\mathrm{eff}||}$ and $\epsilon''_{\mathrm{eff}||}$ for the measured reflection and transmission whereas the blue dots are the retrieved values for reflection and transmission data calculated with a transfer-matrix ansatz. Note that "calculation" in this context always means that we used permittivities of Ag and GaAs from literature.[28] The retrieved values deviate considerably from those obtained in the effective-medium model, indicating that the effective-medium approach is inadequate in the whole spectral range for the given geometrical parameters. We note that due to the inversion process that is needed to obtain $\epsilon'_{\mathrm{eff}||}$ and $\epsilon''_{\mathrm{eff}||}$ from Eqs. (5) and (6) there exist multiple solutions. In Fig. 5(a) we explicitly show the solution which has the smallest deviation from the effective-medium model. That the displayed retrieved values of the real part are all negative is only by chance. There exist also positive solutions but nevertheless the deviation is even larger. We remark that this *does not* imply that the structure has a negative permittivity over the examined energy range. In fact, the experiments demonstrate that there is a transition from metal-like behavior to dielectric behavior. Retrieving the effective permittivities for the structures with $RHL_{0.56}$, $RHL_{0.65}$, and $RHL_{0.74}$ leads to similar results (not shown); however, with increasing layer thickness ratio the effective plasma frequency shifts to higher energies, which is due to the increasing layer thickness ratio η.

In the following we study the cause of the deviations of the effective-medium model from the retrieved data. In Fig. 5(b) we theoretically consider structures with a common total thickness of $d_{\mathrm{tot}} = 204$ nm and common layer thickness ratio $\eta = 0.5$, but different winding numbers of $n = 4$ (corresponding to the individual layer thicknesses of $d_{\mathrm{Ag}} = 17$ nm and $d_{\mathrm{(In)GaAs}} = 34$ nm), $n = 10$ ($d_{\mathrm{Ag}} = 6.8$ nm, $d_{\mathrm{(In)GaAs}} = 13.6$ nm), $n = 50$ ($d_{\mathrm{Ag}} = 1.36$ nm, $d_{\mathrm{(In)GaAs}} = 2.72$ nm), and $n = 100$ ($d_{\mathrm{Ag}} = 0.68$ nm, $d_{\mathrm{(In)GaAs}} = 1.36$ nm). In other words, the structure with winding number $n = 4$ is exactly the structure from Fig. 5(a) which we fabricated experimentally ($RHL_{0.5}$). The other three samples with $n = 10,50,100$, although they have the same total thickness d_{tot} and layer thickness ratio η, have smaller individual layer thicknesses of the Ag and (In)GaAs layers. For these four samples, we calculate the reflection and transmission via the transfer-matrix method. Performing the retrieval using the calculated data yielded $\epsilon'_{\mathrm{eff}||}$ and $\epsilon''_{\mathrm{eff}||}$. We observe that for the 50- and 100-winding structures, comprising very thin individual layer thicknesses, the retrieval leads to permittivities as predicted by the effective-medium model. For the structures with only 4 and 10 windings, with layer thicknesses comparable to those of the fabricated structures, strong deviations occur, indicating that the effective-medium model is no longer suitable to describe the multilayer system. This resembles the findings in Fig. 5(a) for the fabricated structure $RHL_{0.5}$. We wish to note here that the effective-medium model fails, although the individual layer thicknesses of $d_{\mathrm{Ag}} = 17$ nm and $d_{\mathrm{(In)GaAs}} = 34$ nm in the 4-winding case, and $d_{\mathrm{Ag}} = 6.8$ nm and $d_{\mathrm{(In)GaAs}} = 13.6$ nm in

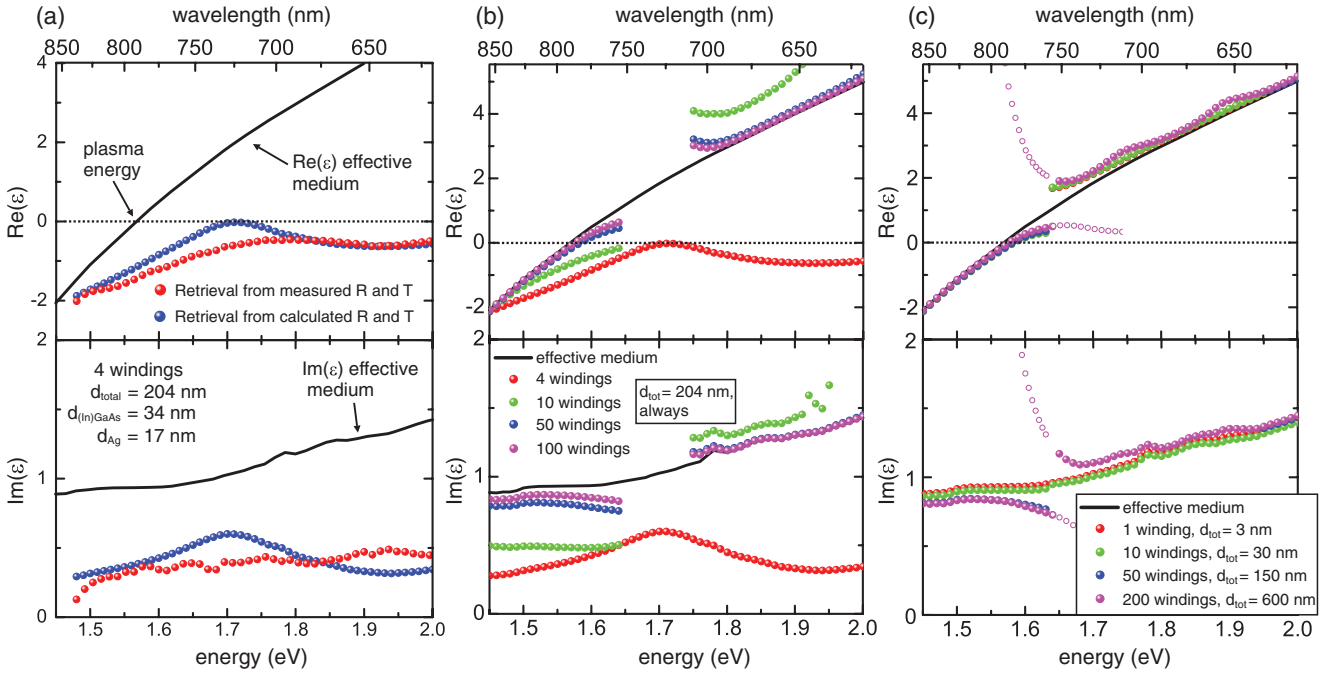

FIG. 5. (Color online) (a) Real (upper graph) and imaginary part (lower graph) of $\epsilon_{\text{eff}||}$ calculated from the effective-medium model (black solid lines), retrieved with transfer-matrix reflection and transmission data (blue dots) and retrieved with measured data (red dots) for the hyperlens $\text{RHL}_{0.5}$ with layer thickness ratio $\eta = 0.5$ [for the R and T data see Fig. 4(a)]. (b) Retrieved real (upper graph) and imaginary (lower graph) parts for a structure with total thickness of $d_{\text{total}} = 204$ nm and layer thickness ratio $\eta = 0.5$, but different winding numbers of $n = 4$, 10, 50, and 100. The reflection and transmission has in each case been calculated by a transfer-matrix ansatz. (c) Retrieved real (upper graph) and imaginary (lower graph) parts for a structure with individual layer thicknesses $d_{\text{Ag}} = 1$ nm and $d_{(\text{In})\text{GaAs}} = 2$ nm ($\text{RHL}_{0.5}$) for winding numbers of $n = 1$, 10, 50, and 200 windings. The circles in the $n = 200$ case exemplarily show how the two solution branches continue and diverge from the effective-medium model.

the 10-winding case, are still considerably smaller than the wavelength of the incident radiation.

To address the influence of the total multilayer thickness we calculated, by using the transfer-matrix method, the reflection and transmission through artificial structures where we kept the individual layer thicknesses constant at $d_{\text{Ag}} = 1$ nm and $d_{(\text{In})\text{GaAs}} = 2$ nm (i.e., $\eta = 0.5$). We again investigated different winding numbers n of $n = 1$, 10, 50, and 200. However, in this case, the change of the winding number means that the total thickness d_{tot} of the structure varies between 3 nm and 600 nm. We performed the retrieval and display the results for the retrieved $\epsilon'_{\text{eff}||}$ and $\epsilon''_{\text{eff}||}$ in Fig. 5(c). We see that in all cases the retrieved permittivities and the permittivity obtained from the effective-medium model are quite similar. We remark that this coincidence still holds for energies even larger than $\hbar\omega = 3$ eV (not shown) and in particular for the structure with $n = 200$ windings, although in this regime the total structure thickness of 600 nm is already larger than the incident wavelength. Also the 200-winding structure in Fig. 5(c) is much thicker than the thickest fabricated structure that we investigated, which gives a strong hint that the individual layer thickness is much more crucial for the validity of the effective-medium model than the total thickness of the structure. This finding is in good agreement with the predictions made in the publication by Rytov.[29] We remark that the slight gap which is observed at an energy of about $\hbar\omega = 1.65$ eV in both Figs. 5(b) and 5(c) arises from two solution branches which are enabled by the inversion of Eqs. (5) and (6). The circles which are exemplarily shown in Fig. 5(c) for the $n = 200$ case depict how these two solution branches continue. It can be observed that they strongly diverge from the effective-medium model. This behavior is similar in all other investigated cases. For reasons of clarity, we displayed it only for one of the investigated samples. Overall our findings show that the effective parameter retrieval is inadequate when applied to structures with individual layer thicknesses larger than 5–10 nm.

VII. FINITE-DIFFERENCE TIME-DOMAIN SIMULATIONS OF HYPERLENSES

Finite-difference time-domain (FDTD) simulations using the commercial software LUMERICAL FDTD SOLUTIONS[35] have been performed to obtain the spatial field distribution for evaluating the hyperlensing behavior of the structures. For convenience, we display the magnetic field distribution that is free of the unsteady boundary conditions at the interfaces. For this purpose, two dipoles emitting radiation coherently at certain energies have been placed in close vicinity of the inner perimeter of the microtubes with a distance of 300 nm from each other. Figure 6(b) shows the magnetic field intensity $|\vec{H}|^2$ in a logarithmic color plot for dipoles emitting at the plasma energy $\hbar\omega = 1.57$ eV for a RHL consisting of 34 alternating layers (i.e., the winding number is $n = 34$) of Ag ($d_{\text{Ag}} = 2$ nm) and GaAs ($d_{\text{GaAs}} = 4$ nm). The structure dimensions have been chosen such that the layer thickness ratio of Ag and GaAs ($\eta = 0.5$) and the total structure thickness ($d_{\text{tot}} = 204$ nm) as

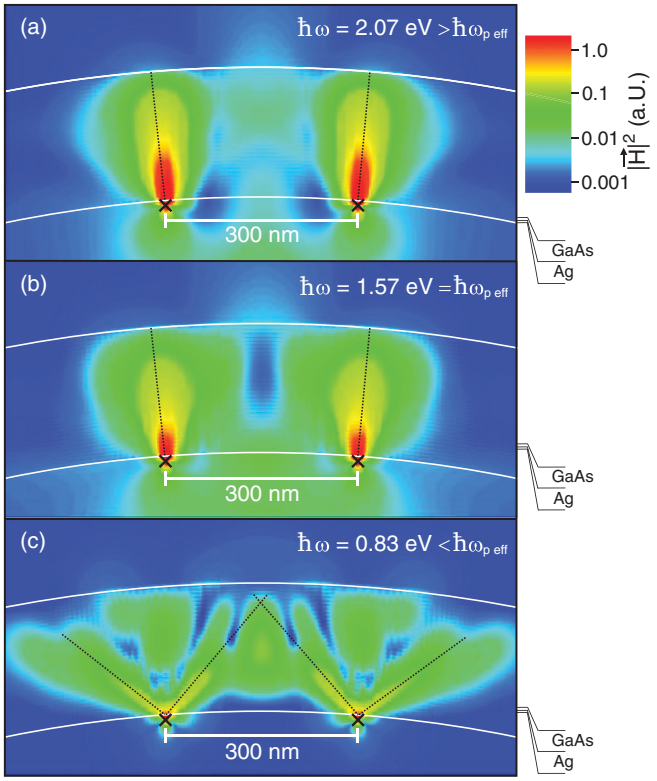

FIG. 6. (Color online) Magnetic field intensity $|\vec{H}|^2$ in a rolled-up metal/semiconductor superlattice containing 34 alternating layers of Ag ($d_{\mathrm{Ag}} = 2\,\mathrm{nm}$) and GaAs ($d_{\mathrm{GaAs}} = 4\,\mathrm{nm}$) obtained from a FDTD simulation (logarithmic plot). Two dipoles with a distance of 300 nm from each other are placed at the inner boundary of the microtube emitting at energies of $\hbar\omega = 2.07\,\mathrm{eV}$ ($\lambda = 600\,\mathrm{nm}$) (a), $\hbar\omega = 1.57\,\mathrm{eV}$ ($\lambda = 790\,\mathrm{nm}$) (b), and $\hbar\omega = 0.83\,\mathrm{eV}$ ($\lambda = 1500\,\mathrm{nm}$) (c).

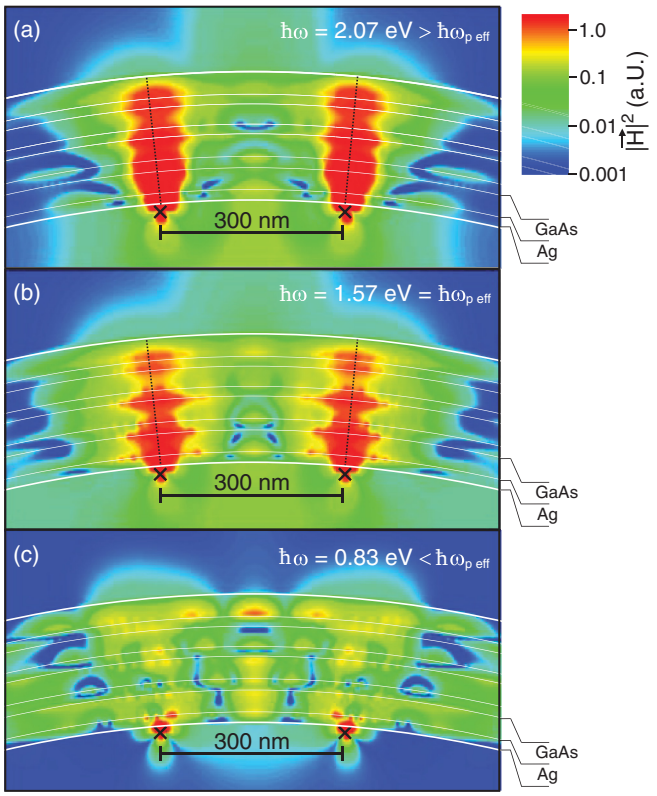

FIG. 7. (Color online) Magnetic field intensity $|\vec{H}|^2$ in a rolled-up metal/semiconductor superlattice containing four alternating layers of Ag ($d_{\mathrm{Ag}} = 17\,\mathrm{nm}$) and GaAs ($d_{\mathrm{GaAs}} = 34\,\mathrm{nm}$) obtained from a FDTD simulation (logarithmic plot). Two dipoles with a distance of 300 nm from each other are placed at the inner boundary of the microtube emitting at energies of $\hbar\omega = 2.07\,\mathrm{eV}$ ($\lambda = 600\,\mathrm{nm}$) (a), $\hbar\omega = 1.57\,\mathrm{eV}$ ($\lambda = 790\,\mathrm{nm}$) (b), and $\hbar\omega = 0.83\,\mathrm{eV}$ ($\lambda = 1500\,\mathrm{nm}$) (c).

well as the tube radius ($r = 2\,\mu\mathrm{m}$) have the same values as for the fabricated $\mathrm{RHL}_{0.5}$. It can be seen that the radiation inside the microtubes is radially channeled. This channeling can be explained within the framework of the effective-medium model. The effective permittivity ($\epsilon_{\mathrm{eff}||} \approx 0.0$ and $\epsilon_{\mathrm{eff}\perp} = 27.1$) is highly anisotropic in this metal/semiconductor structure and a large percentage of the transmitted field components propagates into the same direction as predicted, e.g., in Ref. 8. In Fig. 6(a) the emission energy of the dipoles was changed to $\hbar\omega = 2.07\,\mathrm{eV}$, corresponding to a wavelength of $\lambda = 600\,\mathrm{nm}$. Also in this case, for energies far away from the plasma energy, on the higher-energy side, the channeling behavior is still as distinctive as in Fig. 6(b). The anisotropic character of the effective medium is reduced ($\epsilon_{\mathrm{eff}||} = 5.6$ and $\epsilon_{\mathrm{eff}\perp} = 47$) but is still sufficient to maintain the functionality of the RHL. The idealized RHL is therefore operable not only at the plasma frequency $\omega = \omega_{\mathrm{p\,eff}}$ but also for energies higher than the plasma frequency $\omega > \omega_{\mathrm{p\,eff}}$, supporting the conclusions given in Ref. 33.

However, for energies on the lower-energy side of the plasma frequency ($\hbar\omega = 0.83\,\mathrm{eV}$, corresponding to $\lambda = 1500\,\mathrm{nm}$), where the RHL is in the metallic regime ($\epsilon_{\mathrm{eff}||} = -28.2$ and $\epsilon_{\mathrm{eff}\perp} = 18.1$), no channeling occurs. Instead, as outlined in Ref. 21, the dispersion relation is hyperbolic, with the group velocity having two preferred directions. This behavior can be observed in Fig. 6(c). Two beams (marked with dashed lines) emerge when the radiation emitted from the dipoles propagates in the RHL. We wish to note here that ferromagnetic spin waves exhibit a hyperbolic dispersion relation and are also suitable for subwavelength imaging, as recently shown in Ref. 36. This links the field of spin-wave optics with metamaterials.

In Fig. 7(b) we show the logarithmic magnetic field intensity $|\vec{H}|^2$ of a structure of exactly the dimensions of the $\mathrm{RHL}_{0.5}$ ($d_{\mathrm{Ag}} = 17\,\mathrm{nm}$, $d_{\mathrm{GaAs}} = 4\,\mathrm{nm}$, $r = 2\,\mu\mathrm{m}$, 4 windings). The emission energy of the two dipoles is tuned to the plasma frequency $\hbar\omega_{\mathrm{p\,eff}} = \hbar\omega = 1.57\,\mathrm{eV}$. The individual layer thicknesses are of such size that the magnetic field distribution strongly depends on the location in the RHL, and plasmonic excitations on the metal surfaces occur, indicated by the high magnetic field intensities at the boundaries between the metal and semiconductor layers. Patterns in the field distribution related to the single layers in the RHL become more pronounced with increasing single-layer thickness, thus giving a reason why the effective parameter retrieval is no longer applicable. Nevertheless, it can be seen that the radiation is radially channeled and therefore the fabricated RHL is still expected to support subwavelength imaging.

Interestingly, it turns out that for these large individual layer thicknesses also the hyperlens functionality is preserved over

a broad range of frequencies. This can be seen in Fig. 7(a), which shows the magnetic field intensity distribution at an energy of $\hbar\omega = 2.07\,\text{eV}$ (corresponding to wavelength $\lambda = 600\,\text{nm}$). Comparing Figs. 7(a) and 7(b) with Figs. 6(a) and 6(b), we observe a pronounced radiation channeling in each case. In Fig. 7(c), however, for an energy on the lower-energy side of the plasma frequency ($\hbar\omega = 0.83\,\text{eV}$, corresponding to $\lambda = 1500\,\text{nm}$), the radiation is disorganized as it propagates in the structure. Two emerging beams, as seen in Fig. 6(c), are not observed.

VIII. CONCLUSIONS

In conclusion, we presented detailed investigations of the optical properties of RHLs consisting of alternating layers of Ag and (In)GaAs. By performing reflection and transmission measurements we showed that the RHL exhibits metallic reflection at low photon energies and dielectric transmission at high photon energies. The transmission and reflection data were modeled with transfer-matrix calculations, taking the multilayer structure with its individual layer thicknesses into account. We found deviations which we can attribute to the surface roughness of the thin Ag layers. We experimentally demonstrated that the transition between these two regimes is characterized by the plasma frequency of the RHL which can be tuned in the visible and near-infrared regime by varying the layer thickness ratios between Ag and the (In)GaAs layers. From the experimental data we derived the effective permittivity in the tangential direction and find that the retrieved results differ considerably from those of an effective-medium model for metal/semiconductor superlattices. Our theoretical investigations of the retrieval procedure show that the individual layer thickness of the fabricated RHLs has to be on the order of a few nanometers to achieve coincidence with the effective-medium model. Nevertheless, by performing finite-difference time-domain simulations we showed that subwavelength imaging occurs not only for these very thin layers, but also for layer thicknesses that have been used in the experiments. Additionally, we revealed that for the realized and experimentally investigated structures as well as on optimized structures, efficient subwavelength imaging occurs for energies not only at the effective plasma energy but also for higher frequencies. These findings demonstrate that the functionality of a metamaterial is still obtained when the effective parameter retrieval cannot be used for that material.

ACKNOWLEDGMENTS

We gratefully acknowledge support of the Deutsche Forschungsgemeinschaft via the Graduiertenkolleg 1286 "Functional Metal-Semiconductor Hybrid Systems" and LExI "Nano-Spintronics."

*smendach@physnet.uni-hamburg.de

[1] D. Schurig, J. J. Mock, B. J. Justice, S. A. Cummer, J. B. Pendry, A. F. Starr, and D. R. Smith, Science **314**, 977 (2006).
[2] W. Cai, U. K. Chettiar, A. V. Kildishev, and V. M. Shalaev, Nat. Photonics **1**, 224 (2007).
[3] I. I. Smolyaninov, V. N. Smolyaninova, A. V. Kildishev, and V. M. Shalaev, Phys. Rev. Lett. **102**, 213901 (2009).
[4] T. Ergin, N. Stenger, P. Brenner, J. B. Pendry, and M. Wegener, Science **328**, 337 (2010).
[5] D. Diedrich, A. Rottler, D. Heitmann, and S. Mendach, New J. Phys. **14**, 053042 (2012).
[6] J. B. Pendry, A. J. Holden, D. J. Robbins, and W. J. Stewart, IEEE Trans. Microwave Theory Tech. **47**, 2075 (1999).
[7] D. R. Smith, W. J. Padilla, D. C. Vier, S. C. Nemat-Nasser, and S. Schultz, Phys. Rev. Lett. **84**, 4184 (2000).
[8] S. A. Ramakrishna, J. B. Pendry, M. C. K. Wiltshire, and W. J. Stewart, J. Mod. Opt. **50**, 1419 (2003).
[9] N. Fang, H. Lee, C. Sun, and X. Zhang, Science **308**, 534 (2005).
[10] I. I. Smolyaninov, J. Elliott, A. V. Zayats, and C. C. Davis, Phys. Rev. Lett. **94**, 057401 (2005).
[11] Z. Liu, H. Lee, Y. Xiong, C. Sun, and X. Zhang, Science **315**, 1686 (2007).
[12] J. Rho, Z. Ye, Y. Xiong, X. Yin, Z. Liu, H. Choi, G. Bartal, and X. Zhang, Nat. Commun. **1**, 143 (2010).
[13] R. A. Shelby, D. R. Smith, and S. Schultz, Science **292**, 77 (2001).
[14] A. A. Houck, J. B. Brock, and I. L. Chuang, Phys. Rev. Lett. **90**, 137401 (2003).
[15] G. Dolling, C. Enkrich, M. Wegener, C. M. Soukoulis, and S. Linden, Opt. Lett. **31**, 1800 (2006).
[16] G. Dolling, M. Wegener, C. M. Soukoulis, and S. Linden, Opt. Lett. **32**, 53 (2007).
[17] J. Valentine, S. Zhang, T. Zentgraf, E. Ulin-Avila, D. A. Genov, G. Bartal, and X. Zhang, Nature (London) **455**, 376 (2008).
[18] A. Rottler, M. Harland, M. Bröll, S. Schwaiger, D. Stickler, A. Stemmann, C. Heyn, D. Heitmann, and S. Mendach, Appl. Phys. Lett. **100**, 151104 (2012).
[19] J. B. Pendry, Phys. Rev. Lett. **85**, 3966 (2000).
[20] D. Melville and R. Blaikie, Opt. Express **13**, 2127 (2005).
[21] B. Wood, J. B. Pendry, and D. P. Tsai, Phys. Rev. B **74**, 115116 (2006).
[22] P. A. Belov and Y. Hao, Phys. Rev. B **73**, 113110 (2006).
[23] Z. Jacob, L. V. Alekseyev, and E. Narimanov, Opt. Express **14**, 8247 (2006).
[24] S. Schwaiger, M. Bröll, A. Krohn, A. Stemmann, C. Heyn, Y. Stark, D. Stickler, D. Heitmann, and S. Mendach, Phys. Rev. Lett. **102**, 163903 (2009).
[25] S. Schwaiger, M. Klingbeil, J. Kerbst, A. Rottler, R. Costa, A. Koitmäe, M. Bröll, C. Heyn, Y. Stark, D. Heitmann, and S. Mendach, Phys. Rev. B **84**, 155325 (2011).
[26] A. Rottler, S. Schwaiger, A. Koitmäe, D. Heitmann, and S. Mendach, J. Opt. Soc. Am. B **28**, 2402 (2011).
[27] M. Born and E. Wolf, *Principles of Optics* (Pergamon Press, Oxford, 1980).
[28] E. D. Palik, *Handbook of Optical Constants of Solids* (Academic Press, New York, 1985).
[29] S. M. Rytov, Sov. Phys. JETP **2**, 466 (1956).
[30] D. J. Bergman, Phys. Rep., Phys. Lett. C **43**, 379 (1978).

[31] V. Y. Prinz, V. A. Seleznev, A. K. Gutakovsky, A. V. Chehovskiy, V. V. Preobrazhenskii, M. A. Putyato, and T. A. Gavrilova, Physica E **6**, 828 (2000).

[32] O. G. Schmidt and K. Eberl, Nature (London) **410**, 168 (2001).

[33] J. Kerbst, S. Schwaiger, A. Rottler, A. Koitmäe, M. Bröll, J. Ehlermann, A. Stemmann, C. Heyn, D. Heitmann, and S. Mendach, Appl. Phys. Lett. **99**, 191905 (2011).

[34] Computer code MATHEMATICA, Wolfram Research, http://www.wolfram.com/mathematica/.

[35] Computer code FDTD SOLUTIONS, Lumerical Solutions Inc., http://www.lumerical.com/fdtd.php/.

[36] S. Mansfeld, J. Topp, K. Martens, J. N. Toedt, W. Hansen, D. Heitmann, and S. Mendach, Phys. Rev. Lett. **108**, 047204 (2012).